

Grain-Growth Kinetics of Nanocrystalline Iron Studied In Situ by Synchrotron Real-Time X-ray Diffraction

H. Natter,^{†,§} M. Schmelzer,^{†,§} M.-S. Löffler,^{†,§} C. E. Krill,[†] A. Fitch,[‡] and R. Hempelmann^{*,†,§}

Physikalische Chemie, Technische Physik, Universität des Saarlandes, D-66123 Saarbrücken, Germany, and ESRF, Grenoble, France

Received: May 19, 1999

Pulsed electrodeposition (PED) is used to prepare nanocrystalline iron with an average grain size of 19 nm and thermal stability up to 550 K. At $663\text{ K} \leq T \leq 783\text{ K}$ the kinetics of grain growth, with respect to size and size distribution, is studied in situ by means of real-time synchrotron X-ray diffraction. The Bragg peak line shapes of the large number of diffractograms are analyzed using a Warren/Averbach procedure improved with respect to reliability and efficiency. We observe two regimes of grain growth: at less elevated temperatures grain growth is smooth and moderate up to limiting size values between 50 and 100 nm, depending on temperature. The initially rather narrow width of the size distribution increases slightly, and the activation energy of grain growth, about 100 kJ/mol, corresponds to the literature value for grain boundary self-diffusion in nanocrystalline Fe. At higher temperatures the grains grow first rapidly and then slowly up to limiting values between 200 and 400 nm, depending on temperature. The size distribution becomes rather broad, and the activation energy for grain growth, about 175 kJ/mol, corresponds to the literature value for grain boundary self-diffusion in coarse-grained polycrystalline Fe. We do not find evidence for a change of the type of distribution which indicates normal grain growth. The quality of our diffraction data allows a critical evaluation of different kinetic models of grain growth.

1. Introduction

Nanocrystalline solids consist of crystalline grains with sizes between 5 and 100 nm separated by disordered grain boundary regions.^{1,2} Because of the large volume fraction of interfaces and/or the small crystallite/grain sizes, nanocrystalline solids differ in certain physical properties from coarse-grained polycrystalline solids of the same chemical composition.³ In materials science, this is a novel feature: because certain physical or chemical properties depend—in the nanometer regime—on the grain size or on the interface volume fraction, respectively, the fascinating possibility arises that materials properties can be tuned to desired values simply by adjusting the grain-size appropriately during the production process. Examples of grain size dependent properties are the coercivity and permeability of ferromagnetic transition metals,^{4,5} the hardness of WC/Co hard-metal composites,⁶ enhanced corrosion resistance in nano-Ni,⁷ and increased hardness in nano-Au.⁸

Unquestionably, the grain-size dependence of materials properties is promising for quite a number of applications. During these applications, at the operating temperatures, grain growth must be excluded or at least restricted to an acceptable low level, because otherwise the relevant properties of the corresponding devices change with time during operation. Therefore, sufficient thermal stability with respect to grain growth is the prerequisite of every application of nanocrystalline solids. On one hand, thermal stability can be of thermodynamic origin; this is the case when by appropriate measures (mostly

doping), the excess energy of the interface is reduced to such an extent that there is no longer a driving force for grain growth.⁹ On the other hand, thermal stability can be of kinetic origin, such that by appropriate measures (solute doping atoms or segregates in the grain boundary), the mobility of the grain boundaries is sufficiently reduced.¹⁰ These latter phenomena are often called solute drag or Zener drag, respectively.¹¹ In any case, for a fundamental understanding of thermal stability, accurate experimental studies of the kinetics of grain growth are necessary, and this is the aim of the present contribution.

The grain growth kinetics of conventional *coarse-grained materials* is a well-established field,¹¹ as outlined in section 2. The grain sizes are commonly determined by metallographic techniques or by electron microscopy, i.e., *ex situ*. From grain size histograms mostly comprising only rather small numbers of grains, average grain sizes and sometimes even grain size distributions are deduced, with correspondingly low statistical significance. The new feature of kinetic grain growth studies on *nanocrystalline materials* is the possibility to deduce the size and the size distribution and, additionally, the concomitant microstrain from a line-shape analysis of appropriate Bragg peaks in X-ray diffractograms recorded in situ during the grain growth. The advantage of in situ, as compared to *ex situ*, experiments is obvious: exactly the same part of the sample is studied at all times, and problems of heating-up and cooling-down times do not exist. To exploit this possibility, we have used an X-ray diffractometer based at a synchrotron source, for these reasons: (1) the extreme angular resolution enables us to determine the grain-size-induced line broadening up to grain sizes of about 500 nm, whereas the resolution of a standard laboratory X-ray diffractometer sets an upper limit at about 100 nm, and (2) the high intensity available at a synchrotron source enables us to record a diffractogram in a few minutes with

* To whom correspondence should be addressed. E-mail: hempelmann@rz.uni-sb.de.

[†] Universität des Saarlandes.

[‡] ESRF.

[§] Dedicated to Prof. Dr. Dr. h.c. mult. E. Wicke on the occasion of his 85th birthday.

sufficient count rates; such a time resolution for a real-time experiment of the grain-growth kinetics cannot be reached with a standard laboratory diffractometer.

Taking advantage of these two features of synchrotron X-ray diffractometry, we present in this contribution a detailed experimental study, isothermally at different temperatures, of the temporal evolution of grain size, grain-size distribution, and microstrain of a nanocrystalline metal. Thereby, to our knowledge for the first time, we observe in situ the transition from the nanocrystalline to the polycrystalline grain-growth kinetics. Of essential importance for the present study is the reliability and efficiency of the Bragg peak line shape analyses, which will therefore be described in some detail.

2. Kinetics of Grain Growth

The theoretical basis for understanding grain growth was set forth about 50 years ago in the classic papers of Smith,¹² Burke,¹³ and Burke and Turnbull,¹⁴ who deduced grain growth from the movement of grain boundaries. They assume that the driving pressure on a grain boundary arises from its curvature, which is identified with the mean radius (or diameter, D , respectively) of the grains; then, according to the Kelvin equation, the driving pressure is proportional to the reciprocal radius (or diameter) of the grain:

$$P_{\text{drive}} = \alpha \frac{4\gamma}{D} \quad (1)$$

where α is a small geometric constant. Furthermore, the specific interfacial energy γ is assumed to be the same for all boundaries and to remain unchanged in the course of grain growth. Then the radial velocity of the grain boundary, dD/dt , is proportional to the product of grain boundary mobility, M , and driving pressure:

$$\frac{dD}{dt} \propto MP_{\text{drive}} \quad (2)$$

Hence, combining eqs 1 and 2, for the average grain diameter $D(t)$, one obtains the differential equation

$$\frac{dD(t)}{dt} = \frac{a_1}{D(t)} \quad (3)$$

where the constant a_1 comprises all the above-mentioned quantities; with $D(t) = D_0$ for $t = 0$, the solution of the differential equation is

$$D(t)^2 - D_0^2 = k_1 t \quad (4)$$

D_0 is the initial grain size and $k_1 = 2a_1$, the temperature-dependent rate constant. The last equation is often written in a more general form as

$$D(t)^n - D_0^n = k_1 t \quad (5)$$

which we henceforth shall call the *generalized parabolic grain-growth model*. The empirical grain-growth exponent, n , is in the above analysis equal to 2; such a process is called *parabolic grain growth*. Experimentally, n varies between values of 2 and 4, sometimes even up to 10,¹¹ and for a given system n usually varies with temperature.¹⁵ In any case, in this model the grains continue to grow at long times.

Burke¹³ and later Grey and Higgins¹⁶ took account of the experimental observation of a limiting grain size: in their model, as a result of grain growth, the driving pressure vanishes at a

certain stage; consequently, eq 3 has to be supplemented by a growth-retarding term b_2 :

$$\frac{dD(t)}{dt} = \frac{a_2}{D(t)} - b_2 \quad (6)$$

With the initial grain size D_0 , the solution of eq 6 is

$$\frac{D_0 - D(t)}{b_2} + \frac{a_2}{b_2^2} \ln \left(\frac{a_2 - b_2 D_0}{a_2 - b_2 D(t)} \right) = t \quad (7)$$

At $t \rightarrow \infty$ the grains do not grow anymore, i.e., $dD(t)/dt = 0$; hence $D_\infty = a_2/b_2$ and eq 7 can be expressed as

$$k_2 t = \frac{D_0 - D(t)}{D_\infty} + \ln \left(\frac{D_\infty - D_0}{D_\infty - D(t)} \right) \quad (8)$$

with $k_2 = b_2^2/a_2 = a_2/D_\infty^2$. An expression for $D(t)$ can only numerically be obtained from eq 8, and therefore, in this *grain growth model with impediment*, for the data evaluation it is convenient to fit the reverse function $t(D)$ to the experimental data instead of $D(t)$.

Michels et al.¹⁷ recently suggested that the retardation constant, b_2 , should be a function of the grain size in grain-growth processes of nanocrystalline metals. They argue that in these systems, the impurities in the grain boundaries are more and more enriched when, in the process of grain growth, the grain-boundary volume fraction decreases. The simplest assumption is $b_2 \propto D$, such that

$$\frac{dD(t)}{dt} = \frac{a_3}{D(t)} - b_3 D(t) \quad (9)$$

With the same initial condition as above, the solution of this differential equation is

$$D(t) = \sqrt{\frac{a_3}{b_3} + \left(D_0^2 - \frac{a_3}{b_3} \right) \exp(-2b_3 t)} \quad (10)$$

Using $D_\infty = \sqrt{a_3/b_3}$ this can be expressed as

$$D(t) = \sqrt{D_\infty^2 - (D_\infty^2 - D_0^2) \exp(-k_3 t)} \quad (11)$$

with the rate constant $k_3 = 2b_3 = 2a_3/D_\infty^2$. In the present contribution we shall call this the *grain-growth model with size-dependent impediment*.

As outlined above, the constants $a_{1,2,3}$ contain the product of specific interface energy, γ , and grain boundary mobility, M . In compliance with the fluctuation–dissipation theorem, we relate the mobility of the grain boundary to the self-diffusion coefficient, D_s , in the grain boundary:

$$M = \frac{D_s}{k_B T} \quad (12)$$

where k_B is the Boltzmann constant. In general form eq 12 is known as the Einstein equation. The diffusivity obeys the Arrhenius law with the activation energy, Q , but according to eq 12 the mobility and thus the kinetic rate constants derived above exhibit an additional T^{-1} temperature dependence, such that

$$Tk_{2,3} D_\infty^2 \propto \exp \left(-\frac{Q_{2,3}}{RT} \right) \quad (13)$$

Hence, the activation energies of the grain boundary diffusion processes can be obtained from the slopes of plots of Tk_1 or $Tk_{2,3}D_\infty^2$, respectively, versus T^{-1} ; thereby γ is assumed to be temperature-independent. Concerning the temperature dependence of the retarding terms b , we are not aware of theoretical predictions.

3. X-ray Line-Shape Analysis

Elastic scattering—or, synonymously, diffraction of radiation on matter—mathematically corresponds to a Fourier transformation from real space to momentum space; hence the X-ray diffraction pattern of a sample represents a complete mapping of its structure and its microstructure in momentum space, which is often called reciprocal space or, in the case of periodic structures, reciprocal lattice. In most investigations *structural* information is extracted from the diffraction pattern, namely from the angular positions and intensities of the Bragg peaks. Here, however, we are interested in the *microstructure*, or, more strictly speaking, the nanostructure of our sample. Very roughly, the nanostructure can be quoted by just one quantity, the volume-weighted average size; this information can, in a certain approximation, be derived from the *line widths* of Bragg peaks. Generally, the line width of a Bragg peak of a nanocrystalline material is due to the instrumental width (resolution) of the diffractometer, a broadening due to the small grain size and a broadening due to microstrain. But, as will be described below, more detailed information is accessible in the *line shapes* of Bragg peaks; their evaluation allows us to characterize the nanostructure more thoroughly, in terms of a grain-size distribution and in terms of an isotropic mean-squared microstrain. Thereby “size”, strictly speaking, denotes the size of coherently scattering regions. Stacking faults, for example, cause an apparently reduced grain size if the grain size is calculated from diffraction peaks; because stacking faults are not essential for bcc metals, they are not considered here, and we refer to recent literature.¹⁸

3.1 Size Distribution Function. For nanocrystalline materials, the (normalized) log-normal distribution function has turned out to be appropriate¹ for describing the grain-size distribution:

$$g(D) = \frac{1}{\sqrt{2\pi D \ln \sigma}} \exp \left[-\frac{1}{2} \left(\frac{\ln(D/\mu)}{\ln \sigma} \right)^2 \right] \quad (14)$$

It is characterized by the median diameter, μ , and the geometrical standard deviation, σ . Typical σ -values are: larger than 2 for materials nanoscaled by ball milling,¹⁹ 1.7–1.8 for nanocrystalline metals prepared via inert-gas condensation,²⁰ 1.3–1.4 for nanocrystalline metals prepared by pulsed electrodeposition,^{21,22} 1.1–1.2 for nanocrystalline oxide particles prepared by a sol–gel-type hydrolysis in microemulsion-provided nanoreactors²³ and as low as 1.03 for SiO₂ particles via Stöber synthesis.²⁴ $\sigma = 1$ corresponds to a δ -function. Log-normal distributions are later displayed in Figure 5; characteristic quantities are the area-weighted average grain size $\langle D \rangle_{\text{area}}$ and the volume-weighted average grain size $\langle D \rangle_{\text{vol}}$, as marked in Figure 5, which can be expressed in terms of μ and σ :

$$\langle D \rangle_{\text{area}} = \mu \exp^{5/2 \ln^2 \sigma} \quad (15)$$

$$\langle D \rangle_{\text{vol}} = \mu \exp^{7/2 \ln^2 \sigma} \quad (16)$$

or, vice versa:

$$\mu = \langle D \rangle_{\text{area}}^{7/2} \langle D \rangle_{\text{vol}}^{-5/2} \quad (17)$$

$$\sigma = \exp(\sqrt{\ln(\langle D \rangle_{\text{vol}} / \langle D \rangle_{\text{area}})}) \quad (18)$$

3.2 Column Length. It is well-known that small grain sizes cause a broadening of X-ray diffraction peaks. The primary experimental quantity, however, is the volume-weighted average, $\langle L \rangle_{\text{vol}}$, of so-called column lengths L , i.e., the lengths of columns of cubic cells aligned perpendicular to the set of diffracting lattice planes. The interrelation between grain size and column lengths is visualized in Figure 1 for a spherical particle: the sphere consists of columns with different lengths

$$L = nd^* \quad (19)$$

where d^* is the side length of the cubes; d^* is a fictitious lattice spacing to be explained later, in eq 26.

Even for an ensemble of monodisperse spheres, the column lengths exhibit a distribution; only the central column length equals the particle's diameter, and all other columns are smaller. The primarily obtained average column lengths of an ensemble of particles can be transformed into average grain sizes if all the crystallites in the sample have roughly the same shape;^{25,26} the standard assumption is a spherical shape, then

$$\langle D \rangle_{\text{area}} = \frac{3}{2} \langle L \rangle_{\text{area}} \quad (20)$$

$$\langle D \rangle_{\text{vol}} = \frac{4}{3} \langle L \rangle_{\text{vol}} \quad (21)$$

3.3 Scherrer Formula and Williamson/Hall Plots. For completeness, we briefly mention here the two most-known formalisms for the evaluation of *line widths* of Bragg peaks. Scherrer²⁷ attributed the total width to grain-size effects and obtained for Γ , the full width at half-maximum:

$$\Gamma = \frac{K\lambda}{\cos \theta \langle L \rangle_{\text{vol}}} \quad (22)$$

The Scherrer constant K equals 0.9 for spherical particles. Additionally, taking into account eq 21 (which is not always done in the literature), eq 22 allows, in a very simple way, an estimate of the volume-weighted average grain size, which for small grain sizes (large broadening) and small microstrain is quite reasonable.

The Williamson/Hall technique²⁸ takes into account both size and strain effects. For the separation, the different θ dependences are utilized: The size broadening is proportional to $\cos^{-1} \theta$ (see eq 22), and the strain broadening is proportional to $\tan \theta$; hence, according to

$$\Gamma \cos \theta = \frac{K\lambda}{\langle L \rangle_{\text{vol}}} + 4\epsilon \sin \theta \quad (23)$$

a plot of $\Gamma \cos \theta$ versus $\sin \theta$ enables the separation of microstrain (slope) from the size (ordinate intersection) effects. The additive combination of the two line-broadening contributions in eq 23 implies a Lorentzian line shape for both terms, which, in general, is not the case; therefore, some size average is obtained which is not well defined. In general, the microstrain is anisotropic; therefore, these so-called Williamson/Hall plots have to be done separately for different directions in the reciprocal lattice. An apparently anisotropic grain size might indicate lattice faults. Thus, Williamson/Hall plots exhibit quite direct nanostructural information. In most cases both the

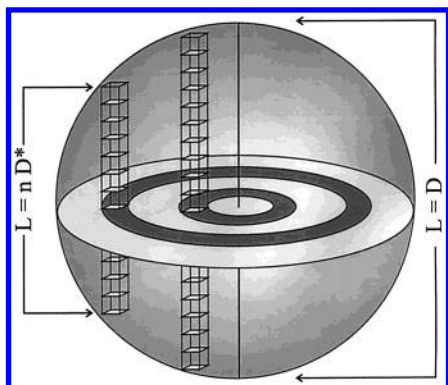


Figure 1. Relation between column length and diameter for a spherical particle.

Scherrer and the Williamson/Hall methods are applied with an approximate deconvolution of the instrumental width. This can be accomplished in a very crude way by simply subtracting the instrumental line width from the experimental one.

3.4 Resolution Correction. Information about the grain-size distribution is contained in the *line shape* of Bragg peaks. The experimentally observed line shape is the convolution of the intrinsic line shape (scattering function) of the sample with the line shape of the diffractometer.²⁹ This so-called resolution function is determined using a standard LaB₆ sample which does not cause any line broadening. Every Bragg peak of LaB₆ is fitted with a Pearson VII function:

$$I(\theta) \propto \left(1 + (2^{1/m} - 1) \left(\frac{2\theta - P_0}{\text{HWHM}} \right)^2 \right)^{-m} \quad (24)$$

Subsequently, the resulting m and HWHM values are empirically parametrized:

$$\text{HWHM}^2 = A \tan P_0^2 + B \tan P_0 + C$$

$$m = DP_0^2 + EP_0 + F$$

In the case of asymmetric instrumental line shapes, a common feature of laboratory X-ray diffractometers, it is advantageous to employ split Pearson VII functions. Using the resulting empirical parameters A , B , C , D , E , and F , an artificial resolution function $R(2\theta)$ can be calculated at any desired 2θ value. For obvious reasons (i.e., Fourier transformation of the data has to be done anyway), the resolution correction is performed by deconvolution in Fourier space, as is explained below.

3.5 Warren/Averbach Method. The Warren/Averbach³⁰ method is a Fourier method; it allows the separation of size and strain effects and enables us to determine the grain-size distribution. The critical step is the Fourier transformation, which is very sensitive to statistical fluctuations in the data, to truncation effects, and to the background level. Therefore—for the original Warren/Averbach method—extremely good counting statistics and a wide angular measuring range are necessary; these requirements, however, contradict those of a real-time diffraction experiment. To reach a good time resolution, only the relevant part of the diffractogram—as narrow as possible—has to be recorded with counting statistics that are just sufficient. As a solution to this dilemma we have developed the following, meanwhile optimized procedure (early versions have been briefly mentioned before):^{31,21,22} every relevant diffraction peak is fitted with a Pearson VII function, and then the resulting fit function is Fourier transformed. The prior fitting step has a number of advantages:

(1) It represents a very efficient smoothing procedure; data with a certain amount of statistical fluctuations can still be handled reliably, i.e., comparatively short measuring times are acceptable.

(2) The fit functions are known from $-\infty$ to $+\infty$, and so truncation effects do not exist.

(3) Overlapping of Bragg peaks—up to a certain degree—is no problem.

(4) The determination of the background level is straightforward.

The disadvantage—inherent in all data fitting—is that the evaluation is biased: if a given Bragg peak is fitted with one Pearson VII function, implicitly a monomodal size distribution is postulated. The fit—apart from smoothing statistical fluctuations—could, however, also erase real physical features in the data. One has to be aware of this risk and carefully check the quality of every fit, for instance by using the χ_r^2 test: χ_r^2 for a certain peak should be only slightly above 1 over a whole series of diffractograms. If χ_r^2 deviates appreciably from 1, then the presumption of monomodality is questionable and a more complex model should be tried, for instance a bimodal distribution, i.e., a fit with two Pearson VII functions.

The fit functions $R(2\theta)$ of the artificial resolution function and $I(2\theta)$ of the experimental intensity of the sample are transformed into functions of the variable $s = (2 \sin \theta)/\lambda$, where the respective Bragg peak is assumed to be centered at s_0 . For the Fourier transformation, both $R(s)$ and $I(s)$ are expressed as Fourier cosine series (the sine terms vanish for even functions):

$$R(s) = \frac{R_0}{2} + \sum_{n=1}^{500} R_n \cos[n\pi(s - s_0)2d^*] \quad (25a)$$

$$I_{hkl}(s) = \frac{I_0}{2} + \sum_{n=1}^{500} I_n \cos[n\pi(s - s_0)2d^*] \quad (25b)$$

The fictitious interplanar distance, d^* , is given by

$$2d^* = \frac{\lambda}{2(\sin \theta_2 - \sin \theta_0)} = \frac{1}{s_2 - s_0} \quad (26)$$

where θ_2 is the upper limit of the evaluation interval; if the lower and upper limits, s_1 and s_2 in terms of the variable s , were chosen strictly according to the periodicity of the lattice, i.e., $s_1 = 0.5 \cdot s_0$ and $s_2 = 1.5 \cdot s_0$, then d^* would be equal to d_{hkl} . The Fourier coefficients are determined from the integrations

$$R_n = 2d^* \int_{s_0-1/2d^*}^{s_0+1/2d^*} R(s) \cos(n\pi(s - s_0)2d^*) \quad n = 0, 1, 2, \dots \quad (27a)$$

$$I_n = 2d^* \int_{s_0-1/2d^*}^{s_0+1/2d^*} I(s) \cos(n\pi(s - s_0)2d^*) \quad n = 0, 1, 2, \dots \quad (27b)$$

For numerical reasons, to minimize truncation effects, we usually chose $\theta_2 = \theta_0 + 20 \cdot \text{HWHM}$, because beyond 20 line widths the Pearson VII function vanishes. Because the experimental intensity, $I(s)$, is the convolution of the scattering function, $A(s)$ with the resolution function, $R(s)$, deconvolution is possible by a division of the Fourier coefficients:

$$A_n^{hkl} = \frac{I_n}{R_n} \quad (28)$$

A_n^{hkl} are the cosine Fourier coefficients of the (resolution-corrected) scattering function of the hkl -Bragg peak. According

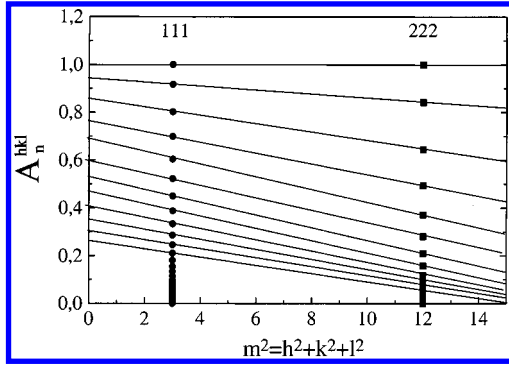


Figure 2. Separation of size and strain effects in the Fourier coefficients in the framework of the Warren/Averbach method.

to Bertaut,³² $n \cdot d^*$, the real-space conjugate variable of $s - s_0$, is identical with the column length, L , discussed in Section 2.2 (see eq 19).

The scattering function, $A(s)$, describes the line-broadening effects of small-particle size and microstrain (macroscopic strain would lead to a change of the lattice constant, i.e., to a shift of the Bragg peak). If size and strain effects are uncorrelated, $A(s)$ is the convolution of both effects. Correspondingly, then, the Fourier coefficients of the scattering function are the product of both terms:

$$A_n^{hkl} = A_n^{\text{size}} A_n^{\text{strain}}(hkl) \quad (29)$$

The size term does not depend on hkl , whereas the strain term does; this allows a separation. Usually, one assumes a Gaussian distributed strain. For small strain, an expansion yields

$$A_n^{hkl} = A_n^{\text{size}} \left(1 - \frac{2\pi^2 \langle \epsilon^2(L) \rangle L^2}{d_{hkl}^2} \right) \quad (30)$$

where $\langle \epsilon^2(L) \rangle$ is the mean-square inhomogeneous strain of a column of lattice cells of length L , which in most cases is anisotropic, i.e., different for different sets of reflections (hkl). In the next step, the Fourier coefficient A_n^{hkl} is normalized such that $A_0^{hkl} = 1$ for all hkl . In this step, all the information contained in the intensity, including the structural information, is lost, but simultaneously all the problems connected with integrated intensities (Lorentz polarization factor, Debye–Waller factor, absorption, etc.) are eliminated. A plot of the normalized Fourier coefficients versus d_{hkl}^{-2} yields the strain-corrected coefficients A_n^{size} as ordinate intersection, as demonstrated in Figure 2. In the case of cubic symmetry one can, according to $d_{hkl}^2 = a^2/(h^2 + k^2 + l^2) = a^2/m^2$ also plot versus m^2 . In general, only Bragg reflections of the same (hkl) set can be used (in the present contribution (110)–(220)), but if in a Williamson/Hall plot the strain has turned out to be small and isotropic, the choice of Bragg reflections is not restricted. Subsequently, the normalized strain-corrected Fourier coefficients are plotted versus the column length $L = nd^*$ as shown in Figure 3. From the initial slope at $L \rightarrow 0$ and from the integration, the area-weighted average column length and the volume-weighted column length, respectively, are obtained:²⁹

$$\left. \frac{dA_n^{\text{size}}}{dL} \right|_{L \rightarrow 0} = - \frac{1}{\langle L \rangle_{\text{area}}} \quad (31)$$

$$\int_0^\infty A_n^{\text{size}} dL = \frac{\langle L \rangle_{\text{vol}}}{2} \quad (32)$$

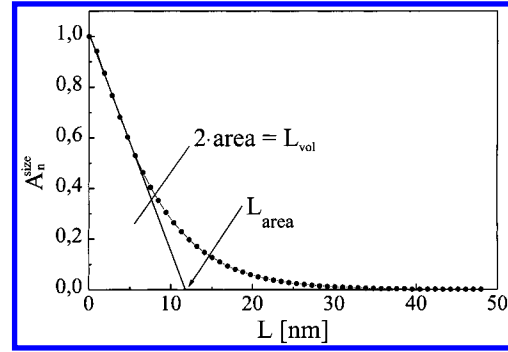


Figure 3. Determination of area- and volume-weighted average column lengths in the framework of the Warren/Averbach method.

According to eqs 20 and 21, average column lengths are transformed into average diameters; then, according to eqs 17 and 18, under the assumption of a log-normal size distribution, the parameters μ and σ , and thus the desired grain size distribution are obtained. Grain sizes below 5 nm cause Bragg peak line widths that are too broad for a reliable evaluation. For standard laboratory diffractometers, the upper grain size that can be evaluated is about 100 nm; otherwise, the line broadening is too small. But with $5 \text{ nm} \leq \langle D \rangle_{\text{vol}} \leq 100 \text{ nm}$, just the nanocrystalline size regime is covered; this explains the importance of X-ray line shape analyses for nanocrystalline materials. A synchrotron-based diffractometer exhibits a much better angular resolution, which extends the measuring range up to 500 nm, as will be shown below.

4. Details of the Synchrotron Experiment

We used the beamline “BM16-Powder Diffraction” of the ESRF in Grenoble (France). This diffractometer is equipped with a primary Si(311) double monochromator, thus providing a variable incident wavelength. We have chosen $\lambda = 0.4898 \text{ \AA}$; at this small wavelength, X-ray absorption in the sample is low. The measuring range was $10^\circ \leq 2\theta \leq 30^\circ$, which corresponds to $0.356 \text{ \AA}^{-1} \leq s \leq 1.057 \text{ \AA}^{-1}$. For bcc iron, this range comprises the (110) up to the (220) Bragg reflection. The measuring time per diffractogram was 1 min; in total, 800 diffractograms have been recorded, but for reason of count statistics we have assembled them into groups of five; hence the “time resolution” of our real-time diffraction experiment was 5 min. The detector system consists of 9 detectors, each with a Si(111) secondary detector in front of it. In this way an angular resolution in 2θ of 0.006° FWHM is reached, more than an order of magnitude better than a common laboratory X-ray diffractometer. The instrumental resolution was determined using a NIST–LaB₆ standard sample in the manner described above.

The nanocrystalline iron sample, which turned out to be brittle, was crushed into a powder using an agate mortar in an Ar glovebox, filled into quartz capillaries ($\varnothing 0.7 \text{ mm}$) and sealed. The diffractograms were recorded in transmission in θ – 2θ mode, at the following temperatures: 663, 683, 703, 739, 753, and 783 K. Sample heating was done by means of a hot-air blower, and the temperature accuracy was $\pm 2 \text{ K}$.

5. Preparation of Nano-Fe by Pulsed Electrodeposition

Since several years PED is applied for the preparation of nanocrystalline metals and alloys, for instance nano-Ni,^{33,22} nano-Pd,³¹ nano-Cu,²¹ nano-Co⁵ or nano-Ni_{1-x}Cu_x.²² For the electrochemical deposition of metals with nanocrystalline microstructure, very small crystallites have to be formed on the

cathode. For that purpose, use is made of the electrochemical version of the Kelvin equation:³⁴

$$r_c = \frac{2\gamma V_m}{ze_0|\eta|} \quad (33)$$

r_c is the critical nucleation radius (i.e., grains with $r > r_c$ are stable), γ the specific surface energy, V_m the atomic volume in the crystal, z the number of elementary charges e_0 , and η the overvoltage.

According to eq 33, the higher the overvoltage, the smaller the crystallites. With the high voltage (about 10 V), a high current (up to 2 A/cm²) is connected, i.e., a very high deposition rate of the metal cations from the electrolyte. The control of this process via eq 33 is possible only for a few milliseconds; after that period, the concentration of metal cations in the vicinity of the cathode is reduced so much that the process becomes diffusion-controlled. To maintain control of the grain size, one has to apply a pulsed current, with correspondingly short pulse widths (a few milliseconds). In the break between two pulses (several tens of milliseconds), metal cations diffuse, as desired, from the bulk of the electrolyte into the vicinity of the cathode. But simultaneously—undesired—on the cathode, due to exchange currents, Ostwald ripening sets in: the somewhat larger grains grow at the expense of the smaller ones. To suppress this exchange process, appropriate organic complex formers are added to the electrolyte bath: the nanocrystals are protected during the break, but complexation is not so strong that metal deposition in the next pulse is impeded.

For the electrochemical preparation of nano-Fe, we use a sacrificial Fe anode and an inert Ti cathode. The electrolyte (citrate bath) contains 50 g/L (NH₄)₂ Fe(SO₄)₂, 20 g/L citric acid trisodium salt, 10 g/L citric acid, and 40 g/L boric acid. The bath temperature is 303 K. With the pulse parameters $t_{\text{on}} = 2$ ms, $t_{\text{off}} = 8$ ms, and $I_{\text{pulse}} = 0.1$ A/cm², we obtain nano-Fe with $\langle D \rangle_{\text{vol}} = 19$ nm and $\sigma = 1.54$. The comparatively moderate pulse parameters are necessary to keep the H₂ evolution, the competing electrochemical reaction, at an acceptable low level. Generally, with very large overvoltage and correspondingly large pulse current density, most of the metallic impurities of the starting materials are co-deposited together with the main constituent; in the present case, however, under the comparatively mild electrochemical conditions described above, a certain electrolytical refinery effect can be expected such that the resulting nanocrystalline iron should contain fewer metallic impurities than the starting materials.

The foil for the anode was 99.5% Fe purchased from Goodfellow, with 3000 wt ppm Mn, 1000 ppm Si, <800 ppm C, and <500 ppm S. The Fe–salt (NH₄)₂ Fe(SO₄)₂ contained <500 ppm Co, <500 ppm Mn, and <500 ppm Ni as main impurities, according to the manufacturer. Chemical analysis of the resulting nano-Fe by means of ICP-MS yields the following (in wt ppm): B 538 ppm, Cr 8.3 ppm, Mn 9.9 ppm, Co 190 ppm, Ni 541 ppm, Cu 33 ppm, Mo 4.4 ppm, Ag 1.0 ppm, Cd 1.2 ppm, and Sn 1.8 ppm; the boron content obviously originates from boric acid in the electrolyte. Chemical analysis of the interstitial impurities in the resulting nano-Fe, by means of hot extraction, gave the following results (in wt %): hydrogen 0.09%, carbon 0.87%, oxygen 1.5%, and nitrogen 0.20%. The closed porosity of our PED–nanometal samples is very low; typical values for the relative bulk density are 97% to 99%, depending on the grain size.²²

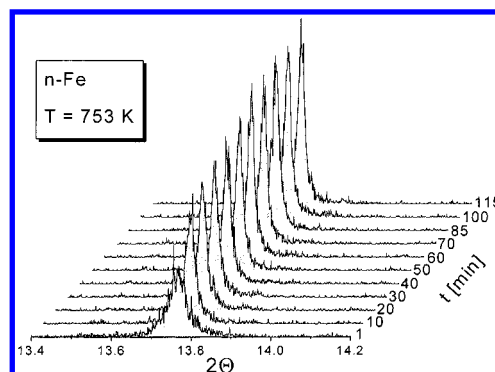


Figure 4. Set of diffractograms of nano-Fe recorded at $T = 753$ K; only the selected angular range is displayed, which comprises the (110) Bragg peak.

TABLE 1: Results of Evaluation of Grain-Size Distributions for Nano-Fe in Initial State and in Final States at the End of the Different Isothermal Real-Time Experiments

T (K)	$\langle D \rangle_{\text{area}}$ (nm)	$\langle D \rangle_{\text{vol}}$ (nm)	μ (nm)	σ	strain (%)
initial	16	19	9.8	1.54	0.684
663	37	46	22.0	1.58	0.303
683	70	92	36.6	1.67	0.201
703	76	103	36.0	1.73	0.179
739	104	150	42.6	1.82	0.103
753	145	234	44.5	1.99	0.076
783	215	395	47.2	2.18	0.023

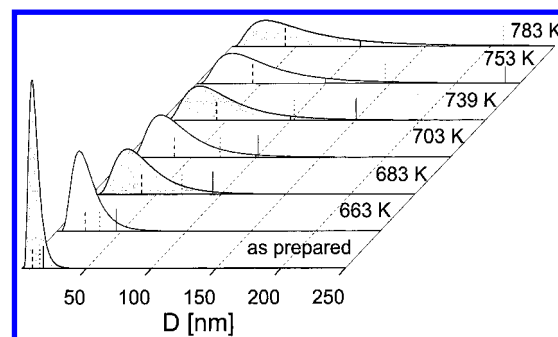


Figure 5. Initial and final grain-size distributions of the different isothermal grain growth experiments on nano-Fe; the dashed/dotted/solid marks indicate the $\mu/\langle D \rangle_{\text{area}}/\langle D \rangle_{\text{vol}}$ values, respectively.

6. Results

Figure 4 shows a selected set of diffractograms recorded at 753 K. We have taken data at five additional temperatures; about 20 diffractograms at each temperature cover a time period of up to 150 min. It can be clearly recognized in Figure 4 that the (110) Bragg peak is broad at the beginning of the real-time isothermal grain-growth experiment, becomes narrow rather quickly, and then, at later times, does not change significantly with time. For the line shape analyses, we used the (110) and the (220) Bragg reflections. The quality of the fits of the profiles with Pearson VII functions is confirmed by the low χ_r^2 values, which exhibit a slight but not significant increase with temperature and time, without any sudden change in between.

In Table 1, the complete results of the evaluation of our primary X-ray diffraction data evaluation are listed for the initial state of our nano-Fe and for the final states at the different temperatures of our experiment. From the primary quantities, $\langle D \rangle_{\text{vol}}$ and $\langle D \rangle_{\text{area}}$, the other quantities have been derived as described in section 2. The median diameter, μ , and the geometrical standard deviation, σ , are used to calculate and visualize the distribution functions in Figure 5: the final medians increase with temperature by a factor of only 2.1, whereas the

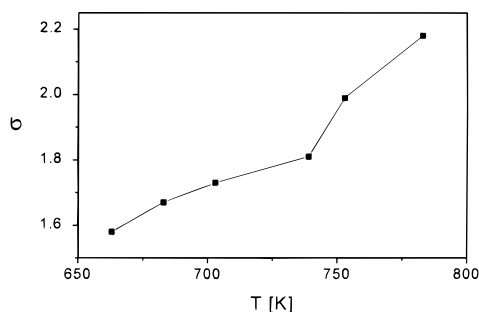


Figure 6. Temperature dependence of the geometrical standard deviations σ of the log-normal distributions of nano-Fe at the end of the different real-time experiments.

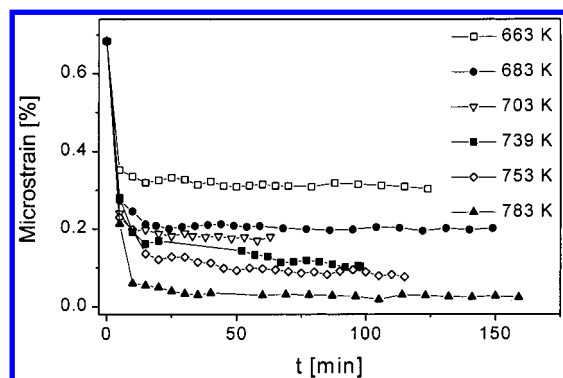


Figure 7. Temperature and time evolution of the microstrain of nano-Fe.

final volume-weighted diameters increase by a factor of 8.6, i.e., the distribution becomes very broad at high temperatures. At $T = 663$ K, isothermally, the median diameter, μ , increases moderately with time, from its initial value of 9.8 nm to, finally, 22 nm. The width parameter, σ , changes, slightly from initially 1.54 to finally 1.58; at $T = 783$ K, the final values are $\mu = 47.2$ nm and $\sigma = 2.18$, indicating a considerable grain growth and a very broad distribution. The final σ values of the different temperature runs are displayed in Figure 6; they exhibit a kind of kink at about 740 K. At the low temperatures, the major changes of both μ and σ occur within the first 10 min; after about 30 min, both μ and σ become more or less time-independent.

In Figure 7, the evolution of the microstrain with time and temperature is displayed. For nano-Fe as prepared, the microstrain amounts to 0.68%; in the isothermal grain growth experiments, this value decreases extremely rapidly right at the beginning and then remains constant at limiting values between 0.3% at 663 K and 0.1% at 753 K. At the highest temperature, 783 K, the microstrain essentially disappears.

The resulting volume-weighted average diameters, $\langle D \rangle_{\text{vol}}$, are displayed as data points in Figure 8; at high temperatures they show a fast increase in the grain size at the beginning of each experiment, and evidently a limiting grain size value at long times, which exhibits a pronounced temperature dependence. At less elevated temperatures, only a moderate and comparatively smooth grain growth is observed, which stops after a short time period.

Fits of the grain sizes with the three kinetic models outlined in section 2 yield the lines in Figure 8 as follows:

(1) The dashed lines are the results of fits with the generalized parabolic grain-growth model, eq 5. The resulting grain-growth exponents n decrease from about 12 at the lowest temperature to about 3 at the highest temperature of our experiments.

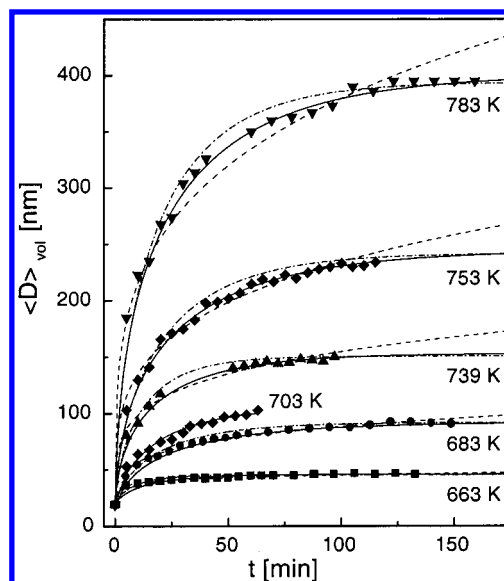


Figure 8. Temperature and time evolution of the volume-weighted average crystallite diameters of nano-Fe; the lines represent fits with different kinetic grain-growth models. Dashed lines represent fits with the generalized parabolic grain-growth model; solid lines represent fits with the grain-growth model with impediment; dashed-dotted lines represent fits with size-dependent impediment.

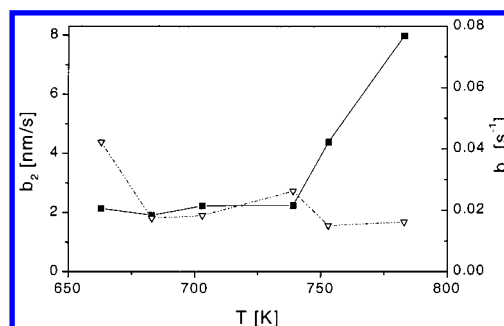


Figure 9. Temperature dependence of the impediment factors. Solid line: from fits with the grain-growth model with impediment; a high temperature and a low temperature regime can clearly be distinguished. Dashed-dotted line: from fits with size-dependent impediment.

(2) The solid lines are the results of the fits with the growth model with impediment, eq 8. The resulting growth-retarding parameter, b_2 , is temperature-independent for $663 \text{ K} \leq T \leq 793 \text{ K}$, but then, for 753 K and 783 K, b_2 clearly increases with temperature as displayed in Figure 9; thus, the two temperature regimes are apparently distinguishable.

(3) The dashed-dotted lines are the results of fits with the grain-growth model with size-dependent impediment, eq 11. The resulting b_3 values amount to about 0.02 s^{-1} for all temperatures except the lowest one, where it is about twice that value (see Figure 9).

All three models contain two adjustable parameters (D_0 is kept fixed at $D_0 = 19 \text{ nm}$). The normalized mean squared residuals

$$\chi_n^2 = \frac{1}{ND_\infty^2} \sum_{i=1}^N (D_i^{\text{exp}} - D_i^{\text{fit}})^2 \quad (34)$$

are plotted in Figure 10 as a function of temperature; at the lowest two temperatures, the generalized parabolic model gives the best fits, but with very high grain growth exponents n ; at medium and high temperatures, the best fits are obtained for

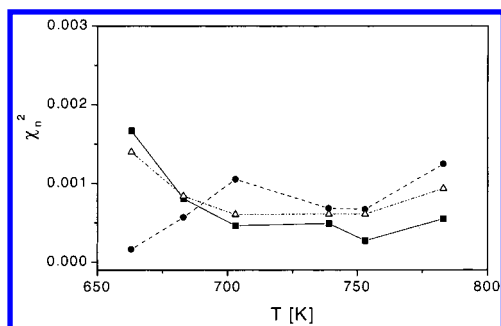


Figure 10. Normalized mean-squared residuals of the fits of Figure 8. Dashed line represent fits with the generalized parabolic grain growth model; solid line represent fits with the grain growth model with impediment; dashed-dotted line represents fits with size-dependent impediment.

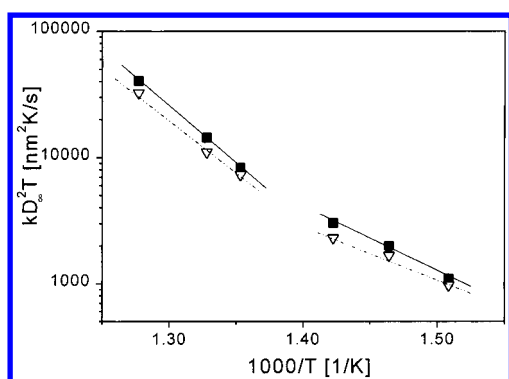


Figure 11. Temperature dependence of the rates a_2 (solid lines) and a_3 (dashed-dotted lines) in extended Arrhenius representations according to eq 13; a high temperature and a low temperature regime can clearly be distinguished.

the model with (constant) impediment. The new model with size-dependent impediment appears to be no improvement; visual inspection of Figure 8 gives this indication, too.

Conventional Arrhenius evaluations of the rates $a_1 = k_1/2$ and $a_{2,3} = k_{2,3}D_\infty^{-2}$ yield activation energies of $Q_1 = 221$ kJ/mol, $Q_2 = 121$ kJ/mol, and $Q_3 = 118$ kJ/mol. There is, however, evidence for deviations from straight-line behavior of a_2 and a_3 . The extended Arrhenius evaluations of these rates, according to eq 13, are displayed in Figure 11. In mutual agreement both model 2, with constant impediment, and model 3, with the retarding term proportional to the size, clearly exhibit different activation energies in the low- and high-temperature regimes, respectively. For the kinetic model 2, we obtain in the high-temperature regime $Q_2^{\text{HT}} = (173 \pm 10)$ kJ/mol, and in the low-temperature regime $Q_2^{\text{LT}} = (98 \pm 8)$ kJ/mol. The corresponding values for model 3 are $Q_3^{\text{HT}} = (165 \pm 10)$ kJ/mol and $Q_3^{\text{LT}} = (84 \pm 8)$ kJ/mol. Conventional, but split, Arrhenius evaluations yield values that are smaller by 6 kJ/mol in the high-temperature regime and by 5 kJ/mol in the low-temperature regime, respectively.

Since the microstrain in n-Fe in the as-prepared state decreases rapidly in the initial stage of grain growth at each temperature (see Figure 7), one could argue that the kinetic modeling should disregard the earliest data point in Figure 8 and treat D_0 as a variable parameter. Then the growth models with impediment and with size-dependent impediment fit the data equally well over the entire temperature range. An Arrhenius evaluation of the resulting rate constants yields activation energies of about 150 kJ/mol for both models without evidence for distinct low and high-temperature regimes.

7. Discussion

Nanocrystalline iron has been prepared by pulsed electrodeposition (PED). By this preparation technique, noble metals with positive standard electrode potential such as Pd³¹ or Cu²¹ can easily be prepared in the nanocrystalline state with low metallic impurity content, low porosity, controlled and adjustable grain size, and comparatively narrow ($1.3 \leq \sigma \leq 1.4$) grain-size distribution. The preparation of nano-Fe by PED, however, is delicate because the Fe standard electrode potential, $E^\circ(\text{Fe}^{2+}/\text{Fe}) = -0.409$ V, is considerably below the standard hydrogen electrode potential, and so H₂ evolution would be the preferential electrochemical process. However, formation of H₂ is strongly impeded at the (growing) Fe cathode due to the large reaction overvoltage of the reaction $2\text{H}_{\text{ads}} \rightarrow \text{H}_2$. To keep H₂ evolution at a low level, compromises in the pulse parameters are necessary, and therefore we have reached only a σ value of 1.54 for our nano-Fe as starting material for the kinetic studies. Still, this means a narrower initial size distribution than can be achieved by other methods, in particular by ball milling (BM),³⁵ the most common method of nano-preparation. Furthermore, PED samples exhibit only a comparatively small amount of lattice strain, in contrast to BM samples, which experience severe plastic deformation during milling.

The content of *metallic impurities* of our PED nano-Fe is low, but *interstitial impurities* such as O, N, and H cannot be avoided, because the preparation takes place in aqueous phase and N₂ gas is bubbled through the electrolyte to drive out O₂. Bulk Fe is intrinsically ductile, but for our nano-Fe we notice a pronounced and (in our view) intergranular brittleness as a result of strong segregation, during the formation process, of interstitial impurities in the grain boundaries. Here these impurities are supposed to enhance the thermal stability of nano-Fe with respect to grain growth; actually, at room temperature and up to 550 K, grain growth is not detectable. For all these reasons we consider our PED-nano-Fe as a well-suited material for a detailed study of grain growth of nanocrystalline metals.

The *experimental method* of choice is in situ synchrotron X-ray diffraction, which to our knowledge has not been used before for investigations of this kind. The novel feature is the possibility to observe the evolution of the (volume-weighted average) *grain size* over more than 1 order of magnitude in size in one experiment; thus, as will be discussed below, the transition from the nanocrystalline regime (5–100 nm) to the polycrystalline regime can be observed; the latter regime is accessible only because of the extreme angular resolution of synchrotron X-ray diffractometers.

Altogether about 800 raw diffractograms have been recorded and for further treatment grouped into 160 diffractograms, each containing about 2000 data points. Only because of the *efficiency of the data evaluation* scheme outlined in section 3 could this huge amount of data be handled and could volume-weighted and area-weighted average diameters be calculated for each diffractogram. From these primarily obtained quantities the size distribution has been calculated for each diffractogram. In this way—and this is also a new feature for a kinetic grain-growth investigation—we could study the temporal evolution of the *size distribution* at different temperatures. We observe a slight increase in the width of the distribution at low temperatures and a rather broad final distribution at high temperatures. Thus we note indications of two different temperature regimes, most clearly from the kink in Figure 6. All data are compatible with a monomodal log-normal distribution, and we find no indication that this type changes in the course of our real-time experiments. We interpret this as evidence for normal grain growth. We would

like to emphasize that with our data evaluation scheme it is possible to detect anomalous grain growth, as we have demonstrated for nano-Ni in a previous ex situ X-ray study.²² Why nano-Fe exhibits normal grain growth and nano-Ni anomalous grain growth is not clear to us at present.

The *microstrain*, $\langle \epsilon^2(L) \rangle$ for $L = D_{\max}$, i.e., for the most frequent diameter, denotes the relative mean-squared deviation of the lattice spacing from its average value. Our PED-nano-Fe in the initial state, as prepared, contains a moderate amount of microstrain, 0.68%. It can be separated into two parts: one part relaxes very rapidly right at the beginning of each temperature run, and the other one obviously does not decay (see Figure 7). We attribute the fast relaxation process to irreversible, local, single-atomic jumps in the grain boundaries; in this way, with one or two jumps, local energetic minima are reached, and the interfacial pressure (see eq 1) on the grains is substantially reduced. The nonrelaxing part of the microstrain apparently depends on the temperature of the experiment. In our view, however, it basically scales with the size of the nanocrystallites (see Table 1) and, as a further experimental observation, it scales with the lattice constant of the nanocrystallites. These findings and their interpretation are the content of a forthcoming publication and are beyond the scope of the present one. Because of the very low porosity in our PED-nanometal samples (see section 5) the pores in our view do not have a significant influence on the grain-growth kinetics.

The *generalized parabolic growth model* fits the data well at low temperatures but with unrealistic, unphysically large grain-growth exponents $n > 10$; the model clearly yields the worst fits at the elevated temperatures (see Figures 8 and 10), although it is mathematically extremely flexible because of the variability of n . For the empirical growth parameters n we obtain values that agree satisfactorily with literature values for BM-nano-Fe of Malow and Koch,¹⁵ Moelle and Fecht,³⁶ and Holzer et al.;³⁷ all these authors used the same model for their data evaluation. The empirical parameters n change from about 12 at low temperatures to about 3 at high temperatures. This could be and has been interpreted as a gradual change of the growth mechanism, but we consider this very indirect hint not as very convincing. The determination of an activation energy for the rate constant k_1 is a problem, because with decreasing n the dimension of k_1 changes dramatically, in our case from nm^{12}/s to nm^3/s , a physically not very appealing situation. As an admittedly questionable measure, we keep $n = 5$ constant in the fit and then obtain an activation energy of 221 kJ/mol, which is in striking disagreement with the values obtained below for the same quantity in terms of the other kinetic models. This value, however, is in accordance with the result of Vandermeer and Huo,³⁸ $Q = 249$ kJ/mol, for grain growth in polycrystalline iron in the temperature range $883 \text{ K} \leq T \leq 1253 \text{ K}$. The activation energy for self-diffusion in iron is 251 kJ/mol^{39,40} and for grain boundary diffusion, 174.5 kJ/mol.^{40,41} In our view, the disagreement of the resulting activation energy with the grain boundary diffusion value and the physically unrealistically large, experimentally determined growth parameters indicate a failure of the generalized parabolic grain growth model to describe grain growth at least in nanocrystalline iron; presumably this statement holds for nanocrystalline metals in general.

The *growth model with impediment* yields the best fits of the three considered models (see Figures 8 and 10). The resulting fit parameters, the retardation term b_2 (Figure 9) and the rate constant $a_2 = k_2 D_\infty^{-2}$ (Figure 11), exhibit—in mutual agreement and in accordance with the width of the grain-size distribution as mentioned above—two temperature regimes. In the high-

temperature regime, the resulting activation energy of the rate constant, $Q_2^{\text{HT}} = (173 \pm 10)$ kJ/mol, agrees perfectly with the activation energy of the grain-boundary self-diffusion coefficient of polycrystalline Fe, $Q = 174.5$ kJ/mol.^{40,41} Actually, apart from the first and second data points, the grain sizes observed in the real-time experiments are outside the nanocrystalline size regime, i.e., they are in the sub- μ -regime. The diffusivity and growth kinetics in this regime correspond to those of polycrystalline materials, and the basic assumption, that grain growth is connected with the mobility of the grain boundaries and thus with the grain-boundary self-diffusion, is quantitatively confirmed. The low-temperature regime of our real-time experiments corresponds to the nanocrystalline size regime. Here the activation energy of the rate constant, $Q_2^{\text{LT}} = (98 \pm 10)$ kJ/mol, is considerably lower, and the absolute value of the rate constant at the lowest temperature of our experiment, $T = 663 \text{ K}$, is nearly an order of magnitude larger than the extrapolated high-temperature value. This is in full accordance with Fe tracer diffusion studies of Tanimoto et al.⁴² on nano-Fe. They observe a considerably enhanced diffusion in the nanocrystalline state with an activation energy of about 109 kJ/mol; the authors interpret their self-diffusion coefficient in terms of grain boundary type-C diffusion kinetics^{40,43} where the volume diffusion in the crystallites is expected to be negligible. The resulting retardation term, b_2 , does not depend on the temperature in the nanocrystalline size regime. Because a higher temperature also means a larger time-averaged size during the run, we conclude that the retardation term seems to be independent of size in the nanocrystalline size regime.

This conclusion is in contradiction with the assumption of Michels et al.¹⁷ in their *growth model with size-dependent impediment*. The parameter b_3 resulting from a fit of our data with this model decreases with temperature at the lowest temperatures of our experiment (see Figure 9) and, as we suppose, in this way in the nanocrystalline state somehow the postulated size dependence is compensated. On the other hand, at higher temperatures the parameter b_3 remains roughly constant, whereas the parameter b_2 increases significantly. The latter behavior seems unphysical, given that the drag on grain-boundary migration exerted by segregated impurities would be expected to remain constant or decrease with increasing temperature.

For both kinetic models with impediment discussed above, disregarding the first data point in Figure 8 leads to an Arrhenius plot with no clear separation into low and high-temperature regimes, primarily because the uncertainties in the low-temperature rate constants are large if D_0 is allowed to vary. A single activation energy is found that is somewhat lower than, but still compatible with, the activation energy for grain-boundary self-diffusion in polycrystalline Fe.

Malow and Koch¹⁵ have performed a kinetic grain growth study on BM-nano-Fe in the temperature range $625 \text{ K} \leq T \leq 875 \text{ K}$ by means of ex situ standard laboratory X-ray diffraction. For evaluation of the line profiles of the Bragg peaks, they use simply the Scherrer equation (eq 22) without taking proper account of the broadening due to lattice strain, which is large in BM samples. The resulting grain sizes approach limiting values at long times, but these values are in striking disagreement with ours (ours are about 1 order of magnitude larger). Also, the resulting kinetic parameters are in such strong disagreement with ours that a comparison does not make sense. We are convinced that Malow and Koch BM-nano-Fe exhibits a kinetic behavior different from our PED-nano-Fe, but in view

of the experimental uncertainties, a quantitative comparison is hardly possible.

Summary

By combining a chemically and nanostructurally well-defined sample (PED-nano-Fe) with a high-performance physical measuring technique (synchrotron X-ray diffraction), we have been able to produce a large amount of high-quality, real-time diffraction data on the grain-growth kinetics of nanocrystalline metals. Using a (primary) data evaluation scheme optimized with respect to reliability and efficiency, we could deduce from these many diffractograms kinetic (secondary) data with such accuracy that a critical comparison with existing kinetic models of grain growth becomes meaningful.

The generalized parabolic grain-growth model exhibits clear deficiencies when applied to comprehensive kinetic data sets of nanocrystalline metals. The grain-growth model with (constant) impediment yields good fits for the isothermal evolution of the grain size with time; furthermore, it enables us to observe a change in the kinetics at the transition from the nanocrystalline to the polycrystalline regime; indicators are both the rate constant and the retardation term. As a strong support for this model, we consider the agreement between the high-temperature activation energy for grain growth and the literature value for the activation energy of the Fe grain-boundary self-diffusion coefficient.

A further new feature of our present study is the determination of grain-size distributions in a real-time experiment. All our data are compatible with a monomodal log-normal grain-size distribution. We observe a slight and gradual increase with time of the median and of the width at low temperatures; at high temperatures, both parameters change rapidly right at the beginning of each real-time experiment and then slowly approach limiting values. We have no indication of a change of the type of distribution, and therefore we diagnose normal grain growth for nanocrystalline iron.

Acknowledgment. The present study was initiated and performed at the University of Saarbrücken in the framework of the "Sonderforschungsbereich 277 Grenzflächenbestimmte Materialien", and we gratefully acknowledge the financial support by the Deutsche Forschungsgemeinschaft. We thank our colleagues in the SFB, L. Helfen for assistance with the synchrotron measurements, Prof. Dr. K.-H. Ehses for stimulating discussions and Prof. Dr. H. Ph. Beck and Dr. K. Ziegler for the chemical analyses. R. H. thanks the Fonds der Chemischen Industrie for generous financial support.

References and Notes

- (1) Granqvist, C. G.; Buhrman, R. A. *J. Appl. Phys.* **1976**, *47*, 2200.
- (2) Gleiter, H. *Prog. Mater. Sci.* **1989**, *33*, 223.
- (3) *Nanomaterials: Synthesis, Properties and Applications*; Edelstein, A. S., Cammarata, R. C., Eds.; IOP Publishing: Bristol and Philadelphia, 1996.
- (4) Herzer, G. *IEEE Trans. Magn.* **1990**, *26*, 1397.
- (5) Schmelzer, M. Ph.D. Thesis, Saarbrücken, 1999.
- (6) Candlish, L. E.; Kear, B. H.; Kim, B. H. *Nanostruct. Mater.* **1992**, *1*, 119.
- (7) Rofagha, R.; Langer, R.; El-Sherik, A. M.; Erb, U.; Palumbo, G.; Aust, K. T. *Scripta Metall. Mater.* **1991**, *25*, 2867.
- (8) Okuda, S.; Tang, F. *Nanostruct. Mater.* **1998**, *10*, 169.
- (9) Erhardt, H.; Krill, C. E.; Birringer, R. In *Chemistry and Physics of Nanostructures and Related Nonequilibrium Materials*; Ma, E., Fultz, B., Shull, R., Morral, J., Nash, P., Eds.; The Minerals, Metals and Materials Society: Warrendale, PA, 1997; p 115.
- (10) Drolet, J. P.; Galibois, A. *Metall. Trans.* **1971**, *2*, 53.
- (11) Humphreys, F. J.; Hatherly, M. *Recrystallization and Related Annealing Phenomena*; Pergamon Press: Oxford, 1996.
- (12) Smith, C. S. *Trans. Metall. Soc. A. I. M. E.* **1948**, *175*, 15. Smith, C. S. In *Metal Interfaces*; ASM, Cleveland 1952; p 65.
- (13) Burke, J. E. *Trans. Metall. Soc. A. I. M. E.* **1949**, *180*, 73; **1950**, *188*, 1324.
- (14) Burke, J. E.; Turnbull, D. *Prog. Metal Phys.* **1952**, *3*, 220.
- (15) Malow, T. R.; Koch, C. C. *Acta Mater.* **1997**, *45*, 2177.
- (16) Grey, E. A.; Higgins, G. T. *Acta Metall.* **1973**, *21*, 309.
- (17) Michels, A.; Krill, C. E.; Erhardt, H.; Birringer, R.; Wu, D. T. *Acta Mater.* **1999**, *47*, 2143.
- (18) Krill, C. E.; Haberkorn, R.; Birringer, R. *Specification of Microstructure and Characterization by Scattering Techniques*. In *Handbook of Nanostructured Materials and Nanotechnology*, Vol. 2; Nalwa, H. S., Ed.; Academic Press: San Diego, 2000, p 155.
- (19) Soetratmo, M. Private communication, 1996.
- (20) Haas, V.; Birringer, R. *Nanostruct. Mater.* **1992**, *1*, 491.
- (21) Natter, H.; Hempelmann, R. *J. Phys. Chem.* **1996**, *100*, 19525.
- (22) Natter, H.; Schmelzer, M.; Hempelmann, R. *J. Mater. Res.* **1998**, *13*, 1186.
- (23) Beck, Ch.; Härtl, W.; Hempelmann, R. *J. Mater. Res.* **1998**, *13*, 3174.
- (24) Beck, Ch.; Härtl, W.; Hempelmann, R. *Angew. Chem.* **1999**, *111*, 1380. Beck, Ch.; Härtl, W.; Hempelmann, R. *Angew. Chem., Int. Ed. Engl.* **1999**, *38*, 1297.
- (25) Smith, W. L. *J. Appl. Crystallogr.* **1976**, *9*, 187.
- (26) Krill, C. E.; Birringer, R. *Philos. Mag. A* **1998**, *77*, 621.
- (27) Scherrer, P. *Göttinger Nachrichten* **1918**, *2*, 98.
- (28) Williamson, G. K.; Hall, W. H. *Acta Metall.* **1953**, *23*, 497.
- (29) Warren, B. E. *X-ray Diffraction*; Dover: New York, 1990.
- (30) Warren, B. E.; Averbach, L. E. *J. Appl. Phys.* **1950**, *21*, 536; **1952**, *23*, 497.
- (31) Natter, H.; Krajewski, T.; Hempelmann, R. *Ber. Bunsen-Ges. Phys. Chem.* **1996**, *100*, 55.
- (32) Bertaut, E. F. *Acta Crystallogr.* **1950**, *3*, 14; **1952**, *5*, 117.
- (33) El-Sherik, A. M.; Erb, U. *J. Mater. Sci.* **1995**, *30*, 5743.
- (34) Budevski, E.; Staikov, G.; Lorenz, W. J. *Electrochemical Phase Transformation and Growth*; VCH: Weinheim, 1996.
- (35) Weeber, A. W.; Bakker, H. *Physica B* **1988**, *153*, 93.
- (36) Moelle, C. H.; Fecht, H. J. *Nanostruct. Mater.* **1995**, *6*, 421.
- (37) Holzer, J. C.; Birringer, R.; Krill, C. E.; Johnson, W. L. *Mater. Res. Soc. Symp. Proc.* **1992**, *272*, 282.
- (38) Vandermeer, R. A.; Hu, H. *Acta Metall. Mater.* **1994**, *42*, 3071.
- (39) *Smithells Metals Reference Book*, 7th ed.; Butterworth-Heinemann: London, 1992; p 13.
- (40) *Diffusion in Solid Metals and Alloys*; Bakker, H., Mehrer, H., Eds.; Landolt-Börnstein New Series Vol. 26; Springer-Verlag: Berlin, 1992.
- (41) Leymonie, C.; Lacombe, P. *Mem. Sci. Rev. Met.* **1959**, *56*, 74. Guiraldenq, P.; Lacombe, P. *Acta Metall.* **1965**, *13*, 51.
- (42) Tanimoto, H.; Farber, P.; Würschum, R.; Valiev, R. Z.; Schaefer, H.-E. *Nanostruct. Mater.* **1999**, *12*, 681.
- (43) Herzig, Ch.; Mishin, Y. *Grain Boundary Diffusion in Metals*; in *Diffusion in Condensed Matter*; Kärger, J., Heitjans, P., Haberlandt, R., Eds.; Vieweg: Braunschweig, 1999.